Soot aggregate restructuring during water processing

Xiaofei Ma [a,b], Christopher D. Zangmeister [b], Julien Gigault [b],
George W. Mulholland [a,b], Michael R. Zachariah [a,b,*]

[a] Departments of Chemical and Biomolecular Engineering and Department of Chemistry and Biochemistry, University of Maryland,
College Park, USA
[b] National Institute of Standards and Technology, Gaithersburg, MD, USA

ABSTRACT

Soot aggregate restructuring is explored in laboratory prepared soot particles upon exposure to high humidity environment followed by rapid water evaporation. Soot was generated in a Santoro style ethylene diffusion burner, and condensation of water on the soot particles was realized in a temperature-controlled water growth tube. The structure transformation of soot particles under different humidity conditions was monitored using a Differential Mobility Analyzer – Aerosol Particle Mass Analyzer (DMA-APM) and Tandem Differential Mobility Analyzer (TDMA) methods. The primary measured properties were mass-mobility scaling exponent, particle mass and mobility size before and after processing. A critical saturation ratio was observed above which aggregate restructuring occurred. The morphological change was visualized by taking electron microscopic images. X-ray photoelectron spectroscopy (XPS) analysis found that the chemical structures of different processed soot were indistinguishable. To assess if soot collapse occurred during water condensation or evaporation, water-coated soot was directly injected into water, where multi-angle light scattering showed that the structure was uncollapsed. This result indicates that soot restructuring driven by capillary forces occurs during evaporation, not condensation.

© 2013 Elsevier Ltd. All rights reserved.

1. Introduction

Soot, a by-product of almost all combustion processes, is the principal light absorbing aerosol in the atmosphere (Bueno et al., 2011). Depending on the source, soot can exist in a variety of shapes, composition, and optical properties. A major question underlying the understanding of the soot climate impact is how the physicochemical properties of individual particles influences aerosol aging, removal mechanisms, residence time in atmosphere, cloud condensation nuclei (CCN) ability, and roles in atmospheric chemistries (Zuberi et al., 2005; Kollensperger et al., 1999). Crucial to soot climate effects is the interaction between soot and water (Zuberi et al., 2005), which can result in water condensation, and result in soot aggregate restructuring, which in turn may lead to changes in optical properties (Zhang et al., 2008).

Soot typically consists of many spherical primary particles which are nearly uniform in size, in a relatively open aggregate structure, comprising a broad size distribution within an aerosol population. Experimental evidence suggests that the surface of the particles have a more ordered graphitic layered structure, where the layer planes are aligned parallel to the surface, with a diminishing graphitic order near the particle center (Donnet et al., 1993). Since soot aggregates are

---

* Corresponding author at: Department of Chemistry and Biochemistry, University of Maryland-College Park, USA.
  E-mail address: mrz@umd.edu (M.R. Zachariah).

fractal-like they are commonly described with a power law:

$$N = k_0 \left(\frac{R_g}{a} \right)^{D_f} \tag{1}$$

where N is the number of primary particles in the aggregates, R_g is the radius of gyration, a is the primary particle size, D_f is the fractal dimension of the aggregate, and k_0 is the pre-factor. Numerous simulations and experiments have provided convincing evidence that soot aggregates obeys the Diffusion Limited Cluster Aggregation law with $D_f = 1.78 \pm 0.1$ and $k_0 = 1.3 \pm 0.2$ (Sorensen, 2011). Direct application of Eq. (1) to determine the fractal dimension requires a measurement of the radius of gyration, typically through TEM, with conversion of a 2-D projected image to a 3-D structure. Additionally, analysis using Eq. (1) usually requires some simplifying assumption about the distribution of primary particle sizes. Light scattering can offer a non-intrusive method to determine the fractal dimension of aggregates (Sorensen, 2001). By plotting the ensemble light scattering intensity versus angle, the radius of gyration from the Guinier and fractal dimension from the power law regime can be obtained (Sorensen, 2001; Kim & Choi, 2003). These methods then provide averaged properties.

On the other hand, the mobility diameter distribution can be measured with high precision a differential mobility analyzer (DMA). McMurry et al. (2002) and Park et al. (2003) developed the DMA-APM technique to characterize agglomerate structure. By measuring the particle mobility diameter d_p, and mass m, over a range of mobility sizes, a power law relationship can be used to extract the mass-mobility scaling exponent D_m of the aerosol population:

$$m \propto d_p^{D_m} \tag{2}$$

Thus D_m contains shape information of the aerosol population. In this study, we employ the mass-mobility scaling exponent as the primary parameter in determining the structural changes to soot particles.

In the simplest picture, soot is composed of hydrophobic primary spherules which are connected via Van der Waals forces (for touching spheres) and/or covalent bonds (for necked spheres). Previous water exposure experiments on freshly emitted diesel soot (Huang et al., 1994; Weingartner et al., 1997), laboratory-generated burner soot (Zuberi et al., 2005; Pagels et al., 2009) and graphite soot by spark discharge (Kollensperger et al., 1999; Mikhailov et al., 2001) have shown only limited restructuring or no restructuring at all.

The propensity of soot to restructure when exposed to water vapor appears to depend on whether the particle can adsorb sufficient water vapor to coat the particle (Bambha et al., 2013). Due to its hydrophobic nature, nascent soot demonstrates little restructuring with exposure to water vapor under sub-saturation conditions (Mikhailov et al., 2001; Miljevic et al., 2012). On the other hand, restructuring upon water condensation/evaporation has been observed experimentally for soot exposed to ozone under UV radiation (Zuberi et al., 2005; Kollensperger et al., 1999; Weingartner et al., 1997), processed by sulfuric acid (Zhang et al., 2008; Pagels et al., 2009) and organic solvents (Mikhailov et al., 2001, 2006). Exposure to supersaturated water vapor can also lead to water uptake and restructuring (Colbeck et al., 1990; Ramachandran & Reist, 1995). The hygroscopic and optical properties of soot can change dramatically due to restructuring and condensation of hygroscopic materials (Zhang et al., 2008; Mikhailov et al., 2006). Soot restructuring has observed with an on-line Tandem Differential Mobility Analyzer (TDMA) (Weingartner et al., 1997) or an APS (Aerodynamic Particle Sizer) (Mikhailov et al., 2001) system measuring the particle size change followed by an ex-situ TEM analysis for fractal dimension measurement. In-situ methods such as Environmental Scanning Electron Microscopy (ESEM) (Ebert et al., 2002) and in-situ Atomic Force Microscopy (AFM) (Kollensperger et al., 1999) are excellent means for visualizing soot morphological changes during processing, but the analysis is limited to a small number of particles, and over a limited range of supersaturation. Furthermore such methods also are affected in unknown ways by substrate effects.

Soot restructuring is usually observed after a complete water condensation/evaporation processes. However due to the difficulty in separating the effects of the two processes experimentally, it is unclear whether it is the water condensation or evaporation process that leads to restructuring.

In this study, we conduct a controlled study to expose both nascent soot and partially oxidized soot to known humidity levels. Restructuring was measured using the DMA-APM technique, and TEM analysis was employed to characterize the soot structure. To separate the effects of condensation or evaporation as the cause of restructuring, static light scattering of water-processed soot (without evaporation) was used to measure the fractal dimension of soot particles collected in water.

2. Experiment

A schematic of the experimental setup is shown in Fig. 1. In brief, the system consists of three components: generation of soot nanoparticles, exposure of soot particles to a supersaturated water vapor concentration, and, finally, measurement of the mass-mobility scaling exponent resulting from water condensation and evaporation.

2.1. Soot generation and sampling

A Santoro style diffusion burner operating on ethylene fuel was used to generate soot particles (Bueno et al., 2011; Santoro et al., 1983). The soot particles were sampled via a sampling method described by Kim et al., (Bueno et al., 2011; Kim et al., 2005) An ejector pump was placed downstream of the sampling system providing dilution and creating
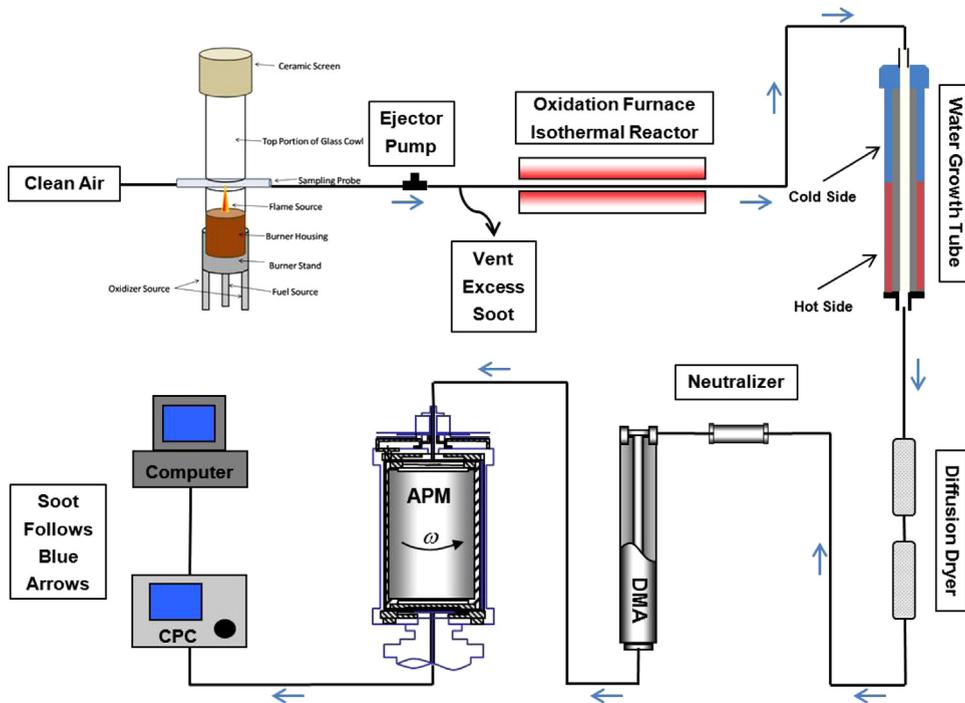
Fig. 1. Schematic of the experimental setup.

a low-pressure region in the direction of the aerosol flow with a pressure drop of approximately 1 kPa. The produced low-pressure drew flow at the flame tip into a 1 mm diameter hole in the sampling probe which was placed orthogonally to the ethylene diffusion flame. Particle-free, dry dilution air was delivered at 5 L/min (L/min) through the sampling probe and mixed with the flame aerosol. In order to increase the soot particle size, the generated soot was allowed to agglomerate in a 5 L accumulation chamber. The aerosol stream flowed from the accumulation chamber to the ejector pump, where additional dilution took place. The final diluted stream was then sampled to create a 1.5 LPM aerosol flow through the rest of the experimental system.

2.2. Soot partial oxidation

Since the hygroscopic properties of soot strongly depend on its surface properties, a tube furnace was placed after the burner to modify the soot's surface by partial oxidation (in dry air) within a $\sim$30 cm (22 mm ID) long heated tube with a residence time of about 5 s. Three temperatures 300 °C, 600 °C and 700 °C were chosen to partially oxidize the soot. The lowest temperature, 300 °C corresponds to what is believed to be the temperature at which most highly volatile organic materials evaporate, but not high enough to initiate the oxidation reaction. DMA-APM measurements showed that soot undergoes only a small mass changes at 600 °C and 700 °C, indicating a partial oxidation process (Ma et al., 2013a).

2.3. Water condensation and evaporation

The main component of the soot processing unit was a commercial water growth tube (Hering & Stolzenburg, 2005; Hering et al., 2005). The detailed operation principles of the growth tube can be found in references (Hering & Stolzenburg, 2005; Hering et al., 2005). Briefly, particles are enlarged through water condensation via a warm, wet-walled condenser in a laminar, thermally diffusive flow. The temperature, T, profile along the centerline are obtained by solution of the partial differential equation,

$$2U\left[1-\left(\frac{r}{R}\right)^2\right]\frac{\partial T}{\partial z}=\alpha_t\frac{1}{r}\frac{\partial}{\partial r}\left(r\frac{\partial T}{\partial r}\right) \tag{3}$$

where r and z are radial and axial coordinates respectively, R is the tube radius, U is average flow velocity, and α_t is the thermal diffusivity of the fluid. The vapor partial pressure, P, profile is governed by the same equation, by replacing the thermal diffusivity with the vapor mass diffusivity. A typical saturation ratio and temperature profile along the growth tube centerline is presented in Fig. 2. The maximum saturation ratio depends on the operating condition of the growth tube and can be calculated from the saturation profile. Two diffusion dryers are placed downstream the ADI growth tube to remove water vapor in the aerosol flow. In the experiment, we varied the saturation ratio inside the ADI growth tube by altering the
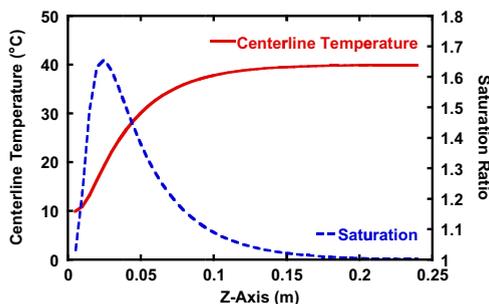
Fig. 2. Temperature and saturation profile inside the growth tube for aerosol flow rate of 1 L/m. $T_{high}=40\ ^{\circ}C$, $T_{low}=10\ ^{\circ}C$.

temperature through the heater and water condenser, and studied the soot structure change as a function of maximum saturation ratio in the growth tube.

2.4. DMA-APM measurement of mass-mobility scaling exponent

The details of the DMA-APM systems have been discussed previously (Ma & Zachariah, 2009, 2010; Ma et al., 2011; Lall et al., 2009; Guha et al., 2012; Liu et al., 2012; Zhou et al., 2008). The DMA which separates particles through a balance of electrostatic and drag forces on a particle, can be used as a band pass filter to generate particles of equivalent mobility size, which should be noted for this work is quite dependent on particle morphology.

The APM operates on the principle of balancing electrostatic and centrifugal forces, can be used as a direct measure of particle mass, independent of morphology (Ehara et al., 1996; Ma et al., 2013b). The DMA-APM combination allows us to using the DMA, mobility-selected particles (which depends on shape), whose mass is then determined by the APM. To determine the mass-mobility scaling exponent of the soot population, the masses of seven different DMA mobility-selected (50–200 nm) soot particles, in increments of 25 nm were measured. By plotting particle mass vs. mobility size, a power law relationship was fit to the data, from which the mass-mobility scaling exponent was extracted (Ma et al., 2012; Zangmeister et al., 2012). In our experiment, the mass-mobility scaling exponent was measured for soot passing through ADI growth tube at different operating conditions.

2.5. TDMA measurement of soot particles

TDMA (tandem DMA) experiments were conducted to measure the particle size change resulting from water condensation and evaporation. In a TDMA setup, DMA1 is used to size select particles, and DMA2 is used to measure the size change of the monodispersed particles resulting from a physical or chemical transformation (Higgins et al., 2002). In our experiment, DMA1 and DMA2 were operated at a sheath flow rate of 10 L/min and 8 L/min air, respectively. Measurements bypassing the growth tube and the diffusion dryers were used to correct for any slight offset between DMA1 and DMA2. TDMA results also served as an independent test for the DMA-APM's mass-mobility scaling exponent measurement. For example, a decrease in particle size is expected if the soot particle collapses due to water condensation and evaporation.

2.6. Static light scattering measurement

The sample for static light scattering measurement was collected using the same water growth tube. The growth tube was operated at a saturator temperature of 45 °C and a condenser temperature of 10 °C with a flow of about 1.5 L/min. The soot aerosol was collected after DMA size selection for about 30 min just downstream of a 2 mm nozzle in a 1 cm diameter vial with about 1 cm^3 water. For static light scattering measurements, about 0.1 cm^3 of the soot suspension is introduced with a syringe into the Wyatt Technology multi-angle light scattering apparatus. The light source is 658 nm, and the light is collected simultaneously at 15 angles ranging from 14° to 160°.

2.7. TEM sample collection and analysis

Samples for electron-microscopic analysis were collected, exiting the diffusion dryers (for sampling the whole aerosol population) or after the first DMA (for sampling size-selected particles) by electrostatically precipitating the aerosol onto a TEM grid (200 mesh copper grids coated with lacey carbon film). A commercial transmission electron microscope was operated at an accelerating voltage of 100 kV to obtain images of particles deposited at different conditions. High resolution TEM images were also taken to determine the primary particle size.

2.8. Soot surface characterization using XPS

Elemental analysis of the soot samples was done on a commercial X-ray photoemission spectroscope (XPS) using a, multichannel-array detector, and a monochromatic Al Kα source with 40 eV pass energy.

3. Results and discussion

3.1. Nascent soot particles

Soot particles generated from the burner, and sampled after the accumulation chamber, as shown in Fig. 3 are fractal-like aggregates with primary particle size about 15–20 nm. The aerosol size distribution, shows a mono-modal distribution with a peak size around 125 nm, was measured with a DMA–CPC (condensation particle counter) system. The mass-mobility scaling exponent of the fresh soot aerosol was determined by the DMA-APM method to be 2.24. From the known relationship between the mobility size and radius of gyration (the details can be found in reference Sorensen (2011)), this value is consistent with a fractal dimension of 1.78 for diffusion limited aggregates.

3.2. Soot structure change as a function of saturation ratio

To elucidate the relationship between soot structural change and saturation ratio the mass of size-selected particles was measured as a function of the maximum saturation ratio inside the growth tube. Aerosol from the burner with a known mobility diameter was passed through the growth tube and dried, following which a certain mobility size was selected by the DMA, and its mass determined by the APM. By operating at fixed mobility size (fixed voltage in DMA), and changing the operating condition of the growth tube, we can obtain the mass evolution of particles with the same mobility size. Structural collapse of a particle can be expected to increase the mass at a given mobility diameter due to the formation of a more compact structure. Figure 4(a) shows a typical mass vs. saturation ratio plot for 150 nm mobility nascent soot particles measured after water condensation and evaporation. Particle mass is observed to be essentially constant with saturation ratio, followed by a jump in mass at a saturation ratio between 1.20 and 1.26, indicating a structure collapse. Further increases in the saturation ratio have negligible effect on particle mass. Similar trends were observed for other size-select particles after exposure to high humidity. The reader is reminded the particles being measured are dry, and thus the increase in APM mass corresponds to a 150 nm mobility particle, which has densified.

By plotting the particle mass against particle size, we can extract the mass-mobility scaling exponent for the whole aerosol population at different growth tube operating conditions. The results are presented in Fig. 5. Each curve represents results under a different saturation ratio. The mass mobility data exhibit a power law relationship, and fall onto two trend lines (two groups of overlapped lines as marked in red and blue). The slope is the mass-mobility scaling exponent. As shown in Fig. 5, for particles exposed to low saturation ratios, the mass-mobility scaling exponent is ~2.24, and thus equivalent to unexposed soot. At higher saturation ratios, a mass-mobility scaling exponent of 2.79 is observed, consistent with a more compact structure. From these results we conclude that our soot restructures into a more compact structure at a critical saturation ratio of 1.20–1.26. It also appears that the critical saturation ratio for soot restructuring is mobility (aggregate) size independent.

The collapsed soot structure was confirmed by TEM analysis. Figure 6(a) and (b) shows images of size-selected 150 nm collapsed soot particles following condensation and subsequent evaporation. Compared to Fig. 3 (nascent soot), soot structural change after water processing is quite evident, and leads in most cases to highly spherical aggregates or relatively uniform in shape. The images of collapsed particles without size-selection are presented in Fig. 6(c) and (d), which shows particles of different sizes restructured into the same spherical shape.

TDMA experiments were conducted to determine the size change between the collapsed soot and its parent nascent particles. Table 1 presents the data for soot particles passing through the growth tube operating at a maximum saturation ratio of 1.48 which is well above the critical saturation ratio for soot structure change. A significant mobility size decrease is
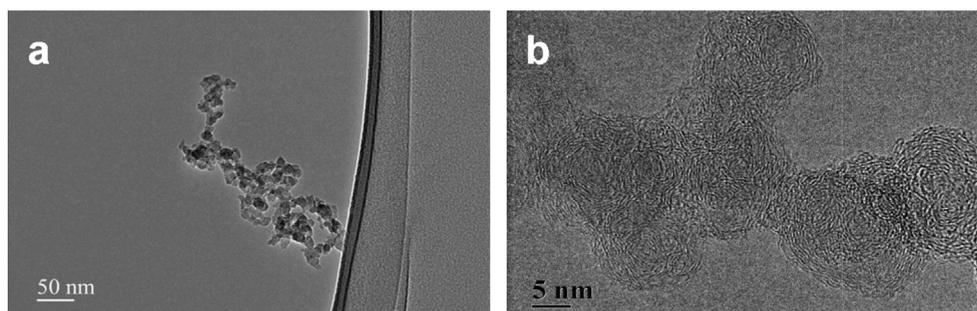

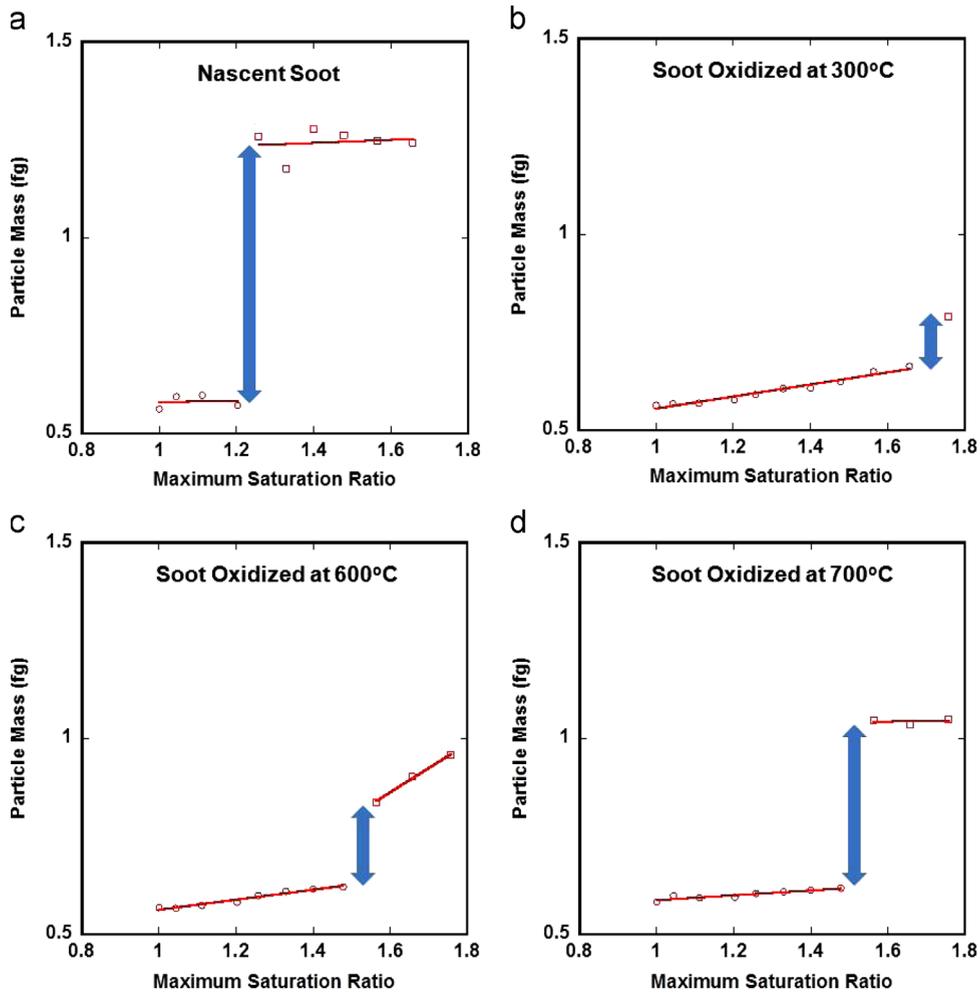**Fig. 3.** TEM images of soot electrostatically deposited to a TEM grid.

Fig. 4. Particle mass as a function of maximum saturation ratio within the growth tube for 150 nm mobility diameter soot particles (Size-selection is after water evaporation and condensation).

observed, which again confirms structural collapse. We also calculated the particle size change assuming a theoretical maximum packing density of 74%. The results are presented in the last column of Table 1. Since the water is removed prior to measurement, the mass of the soot particles should be conserved. The mobility size data is fitting to the following equation:

$$\ln(D_{\mathrm{collapsed}}) = k \ln(D_{\mathrm{nascent}}) + \mathrm{const.} \tag{4}$$

where k is the ratio of the mass-mobility scaling exponent of the collapsed soot to that of the nascent soot and is presented in Fig. 7. A value of 0.803 is obtained for k, which is also equal to the ratio 2.24/2.79 from the DMA-APM method.

3.3. Mechanism of soot structure collapse

The restructuring of aged and processed soot after water condensation and evaporation has been observed by others (Zuberi et al., 2005; Weingartner et al., 1997; Mikhailov et al., 2001). However a significant ambiguity is whether the restructuring occurs during the water uptake or during removal. Ebert et al. (2002) studied the activation of ambient soot using E-SEM and found soot to be more compacted after water evaporation. However, due to the water film formation around the soot particle, their images during water condensation are not clear enough to distinguish structure change. Kollensperger et al. (1999) using in-situ atomic force microscope investigated soot aerosols exposed to different humidities, and found a decrease in particle size occurs during both water condensation and evaporation. It is generally believed that water can condense in small angle cavities of the soot aggregate below 100% humidity due to the Kelvin effect. Soot restructuring then results from unbalanced capillary forces acting on asymmetric portions of a soot aggregate. However, this unbalanced capillary force can exist both during the condensation process and evaporation process. To estimate the magnitude of capillary forces we employ a particle dimer as a simplest component structure in an aggregate (Butt & Kappl, 2009).
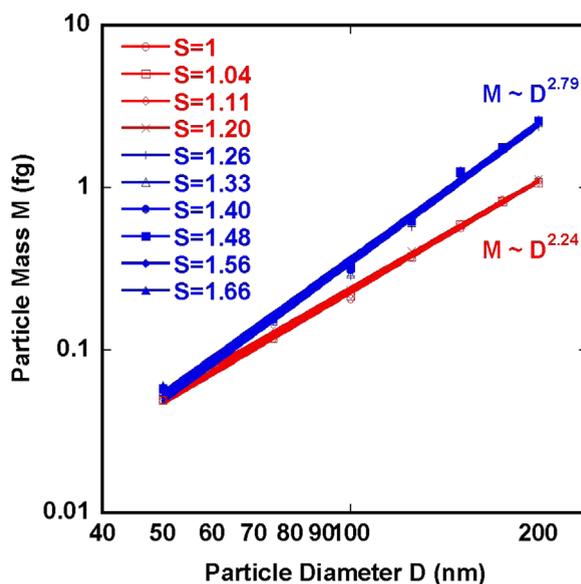
Fig. 5. Particle mass vs. mobility diameter for soot under different growth tube saturation ratios. Note all data for the saturation ratios fall on just these two curves. Red—below critical saturation and blue—above critical saturation (For interpretation of the references to color in this figure legend, the reader is referred to the web version of this article.).
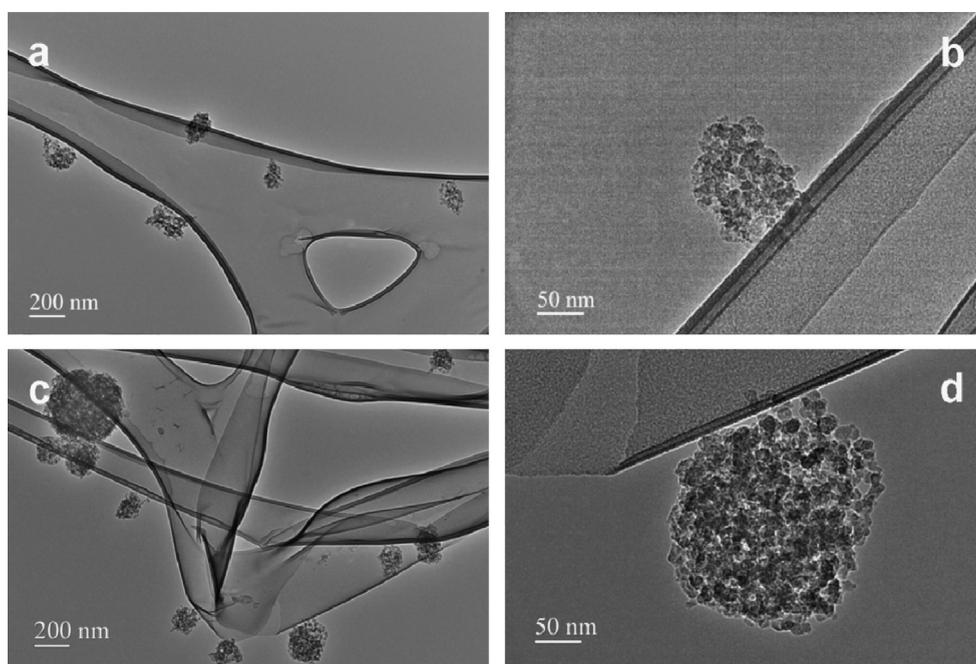

Fig. 6. TEM images of collapsed soot after condensation–evaporation; (a and b) are 150 nm mobility size selected; (c and d) are non-size selected.

In Fig. 8 we show the capillary force as a function of the water-soot contact angle $\varnothing$ and water filling angle β. As we can see from the plot, the capillary force slowly increases with water filling angle, and depending on the contact angle, the capillary force can be positive (attractive force) or negative (repelling force). The magnitude of the capillary force is of the order of nanoNewtons. In comparison, the strength of the Van der Waals force estimated for two touching spheres according to the theory of Hamaker (Israelachvili, 2011).
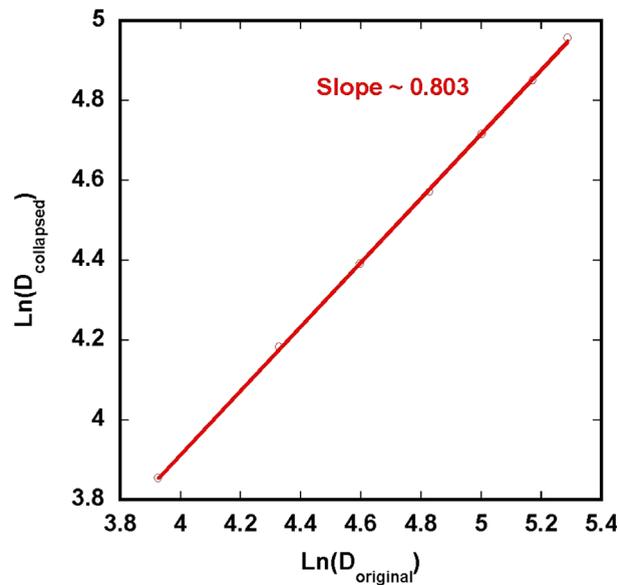
$$F_{\text{Van der Waals}} = A\,\frac{R}{12D^2} \tag{5}$$

where A is Hamaker constant, D is the interparticle distance, and R is the radius of the primary particle. Assuming an interparticle distance $D=0.2$ nm and $A=2\times10^{-19}$ J for soot (Rothenbacher et al., 2008), the calculation shows that the magnitudes of capillary

Table 1
Particle size before and after water condensation and evaporation.

Nominal size (nm)	TDMA nascent soot size (nm)	TDMA soot size at $S=1.48$ (nm)	Percent change in size (%)	Percent size change assuming theoretical maximum packing density (%)
50	50.7	47.2	6.9	14.1
75	75.7	65.6	13.5	23.2
100	99.2	80.7	18.6	29.0
125	125.0	96.7	22.6	33.3
150	148.7	111.8	24.8	36.5
175	176.2	127.9	27.4	40.6
200	198.0	142.2	28.2	43.7

Fig. 7. Collapsed soot mobility size vs. unprocessed soot mobility size on log–log plot.

and Van der Waals forces are of the same order. We conclude then that it is reasonable to expect that particles held by Van der Waals forces will rotate about their contact points due to capillary forces.

In an effort to clarify which process is responsible for the restructuring we needed to make a structural measurement after condensation, but before evaporation. To do this we injected the water condensed soot directly into water to eliminate the capillary effect of evaporation. This enabled us to directly investigate soot structure using multi-angle light scattering. If the results showed a low fractal dimension we could ascribe soot collapse to evaporation, while a large fractal dimension would imply collapse and suggest that condensation triggers restructuring.

The light scattering intensity versus q for different size-selected soot is plotted in Fig. 9. The intensity is normalized by the intensity at 14° and the magnitude of the momentum transfer vector q is defined as

$$q = \frac{4\pi}{\lambda} \sin(\theta/2) \tag{6}$$

The fractal dimension was obtained by linear fitting the sloped region of in the plot. The fractal dimension values were found to be 1.94, 1.45 and 1.63 for 50, 100, and 200 nm soot particles, respectively.

Based on the experiment results, it is quite clear that soot remains open when collected in water. We proposed the following mechanism for soot restructuring. At low saturation ratios (from 1 to 1.20 in our experiment), water condensation is enhanced in small angle cavities of the soot aggregate. The capillary force in the cavities will exert torque on the primary particles and cause them to rotate with respect to each other. This rotation will lead to local compactness of soot aggregate when water is evaporated, which is consistent with the initial slow mass increase in Fig. 4. Above a certain critical saturation ratio, enough water condensation can enclose the whole aggregate. Subsequent water droplet evaporation in the diffusion dryer will lead to soot structure collapse driven by the water surface tension forces exerting on the aggregate core.
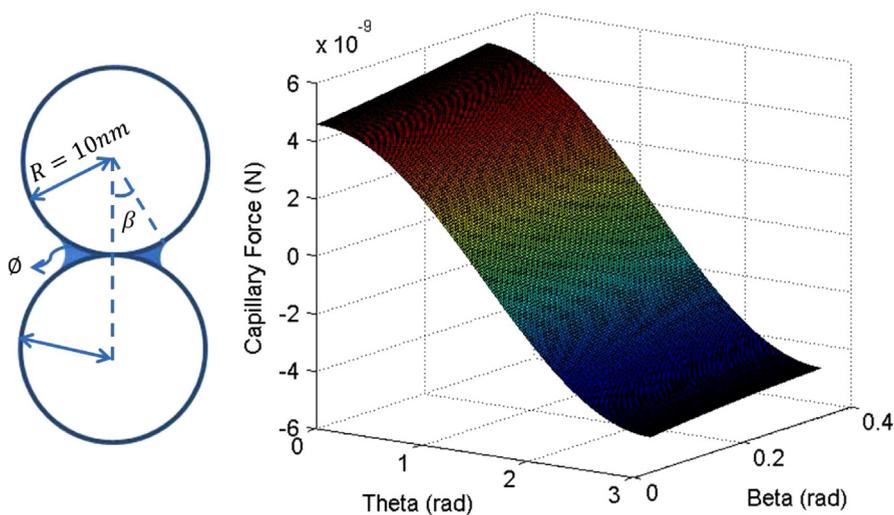
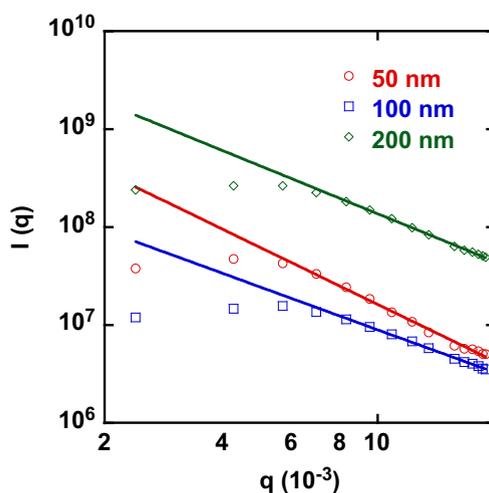Fig. 8. Capillary force between two 20 nm diameter spheres.

Fig. 9. Scattering intensity versus q for size selected soot with a DMA at 50, 100, and 200 nm and then cloud processed, prior to injection into water. The data are corrected for the instruments angular response. Solid lines are best ln–ln fit for the original data minus the 1st four points. The slope of the solid line is the fractal dimension of the particle population.

3.4. Effect of surface properties: hydrophobic vs. hydrophilic effects

It is reasonable to expect that the surface properties of particles will have an effect on the ability to act as water condensation nuclei. In order to study the effect of soot surface properties on water induced structural changes, the soot was first partially oxidized before passing through the growth tube. The critical saturation ratio, which is the lowest saturation ratio required for soot structure collapse, was measured for soot particles oxidized at different temperatures. The results are presented in Fig. 4(b–d). As can be seen from Fig. 4, under the same water condensation conditions, nascent soot underwent the biggest structure change, and required the lowest saturation ratio for structure collapse. While for soot heated at 300 °C, only a small jump in mass was observed at very high saturation ratio (1.65–1.75), indicating a more hydrophobic surface. The critical saturation ratios of structure collapse for soot partially oxidized at 600 °C and 700 °C are almost the same. Furthermore, our measurements of the mass-mobility scaling exponent show that oxidation at 600 °C and 700 °C without water condensation and evaporation does not change the structure of soot.

Since the formation of collapsed soot as demonstrated above is initiated by the removal of water, the growth of condensed water into a droplet that can enclose the soot aggregate plays a key role in this process. Freshly generated aggregates are composed of hydrophobic primary spherules. Various experimental studies on soot-aging processes have shown that oxygenation of the nascent soot surface either by condensation of gaseous organics, H_2SO_4 or by oxidation using

OH, O$_3$, and HNO$_3$ can enhance hydrophilicity (Zuberi et al., 2005; Zhang et al., 2008; Zhang & Zhang, 2005). In order to probe the chemical structure of soot surfaces, XPS analysis was conducted on soot oxidized at different temperatures. However, contrary to our initial thoughts, the XPS results show almost identical surface chemical structure for different processed soot. Thus either subtle changes in surface chemistry are responsible for this observed behavior which XPS is not able to detect, or the oxidation is causing some other effect. One possibility is that oxidation keeps the relative ratio of functional groups essentially constant, but removes high energy (defect) surface sites leading to an effectively "smoother" surface, and thus raising the critical saturation ratio. At this point we have no direct evidence.

4. Conclusions

Structural changes to soot aggregates under water processing was examined using a combination of mobility-mass analysis and static light scattering. The mass-mobility scaling exponent was found to increase from 2.24 to 2.79 upon heterogeneous droplet formation. This was corroborated with TEM analysis which clearly indicated structure collapse. The critical saturation ratio for structural collapse was found to be sensitive to the oxidative environment the soot experienced, but could not be correlated with any significant surface chemical properties as measured by XPS. Finally in order to evaluate if collapse occurred upon drop formation or evaporation, coated particles were directly injected into water, where multi-angle light scattering indicated the fractal dimension remained low. This latter result implies that soot restructuring occurs upon evaporation, and based on force-balance scaling arguments can be attributed to capillary effects.

References

Bambha, R.P., Dansson, M.A., Schrader, P.E., & Michelsen, H.A. (2013). Effects of volatile coatings and coating removal mechanisms on the morphology of graphitic soot. *Carbon, 61*, 80–96.

Bueno, P.A., Havey, D.K., Mulholland, G.W., Hodges, J.T., Gillis, K.A., Dickerson, R.R., & Zachariah, M.R. (2011). Photoacoustic measurements of amplification of the absorption cross section for coated soot aerosols. *Aerosol Science and Technology, 45*, 1217–1230.

Butt, H.J., & Kappl, M. (2009). Normal capillary forces. *Advances in Colloid and Interface Science, 146*, 48–60.

Colbeck, I., Appleby, L., Hardman, E.J., & Harrison, R.M. (1990). The optical properties and morphology of cloud-processed carbonaceous smoke. *Journal of Aerosol Science, 21*, 527–538.

Donnet, J.-B., Bansal, R.C., & Wang, M.-J. (1993). *Carbon Black Science and Technology*. Marcel Dekker, INC.: New York.

Ebert, M., Inerle-Hof, M., & Weinbruch, S. (2002). Environmental scanning electron microscopy as a new technique to determine the hygroscopic behaviour of individual aerosol particles. *Atmospheric Environment, 36*, 5909–5916.

Ehara, K., Hagwood, C., & Coakley, K.J. (1996). Novel method to classify aerosol particles according to their mass-to-charge ratio – Aerosol particle mass analyser. *Journal of Aerosol Science, 27*, 217–234.

Guha, S., Ma, X., Tarlov, M.J., & Zachariah, M.R. (2012). Quantifying ligand adsorption to nanoparticles using tandem differential mobility mass analysis. *Analytical Chemistry, 84*, 6308–6311.

Hering, S.V., & Stolzenburg, M.R. (2005). A method for particle size amplification by water condensation in a laminar, thermally diffusive flow. *Aerosol Science and Technology, 39*, 428–436.

Hering, S.V., Stolzenburg, M.R., Quant, F.R., Oberreit, D.R., & Keady, P.B. (2005). A laminar-flow, water-based condensation particle counter (WCPC). *Aerosol Science and Technology, 39*, 659–672.

Higgins, K.J., Jung, H.J., Kittelson, D.B., Roberts, J.T., & Zachariah, M.R. (2002). Size-selected nanoparticle chemistry: Kinetics of soot oxidation. *Journal of Physical Chemistry A, 106*, 96–103.

Huang, P.F., Turpin, B.J., Pipho, M.J., Kittelson, D.B., & McMurry, P.H. (1994). Effects of water condensation and evaporation on diesel chain-agglomerate morphology. *Journal of Aerosol Science, 25*, 447–459.

Israelachvili, J.N. (2011). *Intermolecular and Surface Forces*. Academic Press, Waltham, MA.

Kim, H.W., & Choi, M. (2003). In situ line measurement of mean aggregate size and fractal dimension along the flame axis by planar laser light scattering. *Journal of Aerosol Science, 34*, 1633–1645.

Kim, S.H., Fletcher, R.A., & Zachariah, M.R. (2005). Understanding the difference in oxidative properties between flame and diesel soot nanoparticles: The role of metals. *Environmental Science & Technology, 39*, 4021–4026.

Kollensperger, G., Friedbacher, G., Kotzick, R., Niessner, R., & Grasserbauer, M. (1999). In-situ atomic force microscopy investigation of aerosols exposed to different humidities. *Fresenius Journal of Analytical Chemistry, 364*, 296–304.

Lall, A.A., Ma, X., Guha, S., Mulholland, G.W., & Zachariah, M.R. (2009). Online nanoparticle mass measurement by combined aerosol particle mass analyzer and differential mobility analyzer: comparison of theory and measurements. *Aerosol Science and Technology, 43*, 1075–1083.

Liu, Q., Ma, X., & Zachariah, M.R. (2012). Combined on-line differential mobility and particle mass analysis for determination of size resolved particle density and microstructure evolution. *Microporous and Mesoporous Materials, 153*, 210–216.

Ma, X., Zangmeister, C.D., & Zachariah, M.R. (2013a). Soot oxidation kinetics: a comparison study of two tandem ion-mobility methods. *The Journal of Physical Chemistry C, 117*, 10723–10729.

Ma, X., Zachariah, M.R., & Zangmeister, C.D. (2013b). Reduction of suspended graphene oxide single sheet nanopaper: the effect of crumpling. *The Journal of Physical Chemistry C, 117*, 3185–3191.

Ma, X.F., & Zachariah, M.R. (2009). Oxidation anisotropy and size-dependent reaction kinetics of zinc nanocrystals. *Journal of Physical Chemistry C, 113*, 14644–14650.

Ma, X., & Zachariah, M.R. (2010). Size-resolved kinetics of Zn nanocrystal hydrolysis for hydrogen generation. *International Journal of Hydrogen Energy, 35*, 2268.

Ma, X., Lall, A.A., Mulholland, G.W., & Zachariah, M.R. (2011). Evaporation anisotropy of free nanocrystals. *Journal of Physical Chemistry C, 115*, 16941–16946.

Ma, X.F., Zachariah, M.R., & Zangmeister, C.D. (2012). Crumpled nanopaper from graphene oxide. *Nano Letters, 12*, 486–489.

McMurry, P.H., Wang, X., Park, K., & Ehara, K. (2002). The relationship between mass and mobility for atmospheric particles: a new technique for measuring particle density. *Aerosol Science and Technology, 36*, 227–238.

Mikhailov, E.F., Vlasenko, S.S., Kramer, L., & Niessner, R. (2001). Interaction of soot aerosol particles with water droplets: influence of surface hydrophilicity. *Journal of Aerosol Science, 32*, 697–711.

Miljevic, B., Surawski, N.C., Bostrom, T., & Ristovski, Z.D. (2012). Restructuring of carbonaceous particles upon exposure to organic and water vapours. *Journal of Aerosol Science, 47*, 48–57.

Mikhailov, E.F., Vlasenko, S.S., Podgorny, I.A., Ramanathan, V., & Corrigan, C.E. (2006). Optical properties of soot-water drop agglomerates: an experimental study. *Journal of Geophysical Research: Atmospheres, 111*.

Park, K., Cao, F., Kittelson, D.B., & McMurry, P.H. (2003). Relationship between particle mass and mobility for diesel exhaust particles. *Environmental Science and Technology*, *37*, 577–583.

Pagels, J., Khalizov, A.F., McMurry, P.H., & Zhang, R.Y. (2009). Processing of soot by controlled sulfuric acid and water condensationmass and mobility relationship. *Aerosol Science and Technology*, *43*, 629–640.

Ramachandran, G., & Reist, P.C. (1995). Characterization of morphological changes in agglomerates subject to condensation and evaporation using multiple fractal dimensions. *Aerosol Science and Technology*, *23*, 431–442.

Rothenbacher, S., Messerer, A., & Kasper, G. (2008). Fragmentation and bond strength of airborne diesel soot agglomerates. *Particle and Fibre Toxicology*, *5*.

Santoro, R.J., Semerjian, H.G., & Dobbins, R.A. (1983). Soot particle measurements in diffusion flames. *Combustion and Flame*, *51*, 203–218.

Sorensen, C.M. (2011). The mobility of fractal aggregates: a review. *Aerosol Science and Technology*, *45*, 765–779.

Sorensen, C.M. (2001). Light scattering by fractal aggregates: a review. *Aerosol Science and Technology*, *35*, 648–687.

Weingartner, E., Burtscher, H., & Baltensperger, U. (1997). Hygroscopic properties of carbon and diesel soot particles. *Atmospheric Environment*, *31*, 2311–2327.

Zangmeister, C.D., Ma, X., & Zachariah, M.R. (2012). Restructuring of graphene oxide Sheets into monodisperse nanospheres. *Chemistry of Materials*, *24*, 2554–2557.

Zhang, D., & Zhang, R.Y. (2005). Laboratory investigation of heterogeneous interaction of sulfuric acid with soot. *Environmental Science and Technology*, *39*, 5722–5728.

Zhang, R., Khalizov, A.F., Pagels, J., Zhang, D., Xue, H., & McMurry, P.H. (2008). Variability in morphology, hygroscopicity, and optical properties of soot aerosols during atmospheric processing. *Proceedings of the National Academy of Sciences of the United States of America*, *105*, 10291–10296.

Zhou, L., Rai, A., Piekiel, N., Ma, X., & Zachariah, M.R. (2008). Ion-mobility spectrometry of nickel nanoparticle oxidation kinetics: application to energetic materials. *The Journal of Physical Chemistry C, 112*, 16209–16218.

Zuberi, B., Johnson, K.S., Aleks, G.K., Molina, L.T., & Laskin, A. (2005). Hydrophilic properties of aged soot. *Geophysical Research Letters*, *32*.